slowly (that is, the major 3° amide rotamer H_E signals broaden in Fig. 4A, c. There is no ambiguity in the macrocycle assignment in *Z*,*E*-**3** because of the visible presence of different 3° amide rotamers). Moving the macrocycle from the 2° amide fumaramide station in *E*,*E*-**3** to the succinic amide ester station in *Z*,*E*-**3** (during which the pirouetting frequency of that macrocycle increases) thus causes the rate of pirouetting of the other macrocycle to decrease, attributed by molecular modelling (Supplementary Information) to the different hydrogen-bonding patterns in the various [3]catenanes. Using stimuli-induced mechanical movement in one component to induce or influence dynamics in another is still rare in synthetic molecular systems[18], yet it is the principle which underpins the workings of all macroscopic machines with moving parts. □

Methods

Kinetic studies on model [2]rotaxanes

The small rings in a [3]catenane will only undergo unidirectional rotation if the 'blocking' ring is effectively translationally immobile over the time period that the other ring moves. If that is not the case, then instead of a single macrocycle moving counter-clockwise during a particular step, both small rings could move clockwise (one displacing the other), or a combination of these could occur throughout the reaction sequence, removing the directionality of the motion. To show that the components of **3** undergo unidirectional rotation over a range of conditions, the contributions of these processes were estimated from the kinetics of various model compounds (Supplementary Information). The energy barriers for a benzylic amide macrocycle to move from each type of station (**A** and **B**, **C**, **D**, **A**′ and **B**′) to another station 12 carbon atoms away at 298 K in $CDCl_3$ were experimentally determined in symmetrical two-station [2]rotaxanes by variable-temperature ^{1}H NMR spectroscopy. The benzophenone unit was shown not to significantly slow shuttling using another model [2]rotaxane. The experimentally determined barriers (fumaramide and *bis*-*N*-methyl fumaramide 16.2 ± 0.4 kcal mol^{-1}; succinic amide ester 11.3 ± 0.2 kcal mol^{-1}; amide $<$ 8 kcal mol^{-1}; maleamide and *bis*-*N*-methyl maleamide $\ll$ 8 kcal mol^{-1}) mean that at 298 K in $CDCl_3$ stations **A** and **B** decomplex, and the macrocycle moves to the next station, 4,000 times less frequently than **C** and $>10^6$ times less frequently than **D**, **A**′ and **B**′ (the ratio of rates is given by $e^{(\Delta\Delta G^{\ddagger}/k_B T)}$). Thus, starting from *E*,*E*-**3**, when **A** is isomerized to **A**′ the macrocycle initially at **A**′ will move to **C** (overcoming two barriers of less than 8 kcal mol^{-1}) to arrive at the equilibrium position of *Z*,*E*-**3** at least a million times more often than the macrocycle originally at **B** moving to **C** (barrier of 16.2 kcal mol^{-1}) and the macrocycle originally at **A** moving to **B**. Similarly, movement of the macrocycle from the **B**′ station to **D** to give the most stable positional isomer of *Z*,*Z*-**3** will occur three orders of magnitude faster than macrocycles moving from **C** to **D** and **B**′ to **C**. Finally, as long as the *N*-methyl maleamide station is not isomerized to the fumaramide unit (**B**′ → **B**) at a significantly faster rate than the secondary maleamide station (**A**′ → **A**) as *Z*,*Z*-**3** is converted to *E*,*E*-**3** (the rates we observe experimentally are the same for both stations), then the macrocycle initially at **D** will move rapidly to **A** where it will be bound tightly and therefore be thousands of times slower to move to the vacant **B** station than the macrocycle originally at **C**. While it is always possible that the inter-station dynamics in the model compounds differ to those in the [3]catenane, the kinetics suggest overwhelming directionality for the stimuli-induced motion in **3** over a wide range of conditions.

Received 19 February; accepted 21 May 2003; doi:10.1038/nature01758.

1. Schliwa, M. (ed.) *Molecular Motors* (VCH-Wiley, Weinheim, 2003).
2. Balzani, V., Credi, A., Raymo, F. M. & Stoddart, J. F. Artificial molecular machines. *Angew. Chem. Int. Edn* **39,** 3348–3391 (2000).
3. Kelly, T. R., De Silva, H. & Silva, R. A. Unidirectional rotary motion in a molecular system. *Nature* **401,** 150–152 (1999).
4. Kelly, T. R., Silva, R. A., De Silva, H., Jasmin, S. & Zhao, Y. A rationally designed prototype of a molecular motor. *J. Am. Chem. Soc.* **122,** 6935–6949 (2000).
5. Koumura, N., Zijlstra, R. W. J., van Delden, R. A., Harada, N. & Feringa, B. L. Light-driven monodirectional molecular rotor. *Nature* **401,** 152–155 (1999).
6. Feringa, B. L., Koumura, N., van Delden, R. A. & ter Wiel, M. K. J. Light-driven molecular switches and motors. *Appl. Phys. A* **75,** 301–308 (2002).
7. Koumura, N. L., Geertsema, E. M., van Gelder, M. B., Meetsma, A. & Feringa, B. L. Second generation light-driven molecular motors. Unidirectional rotation controlled by a single stereogenic center with near-perfect photoequilibria and acceleration of the speed of rotation by structural modification. *J. Am. Chem. Soc.* **124,** 5037–5051 (2002).
8. van Delden, R. A., Koumura, N., Harada, N. & Feringa, B. L. Unidirectional rotary motion in a liquid crystalline environment: Color tuning by a molecular motor. *Proc. Natl Acad. Sci. USA* **99,** 4945–4949 (2002).
9. Sauvage, J.-P. & Dietrich-Buchecker, C. (eds) *Molecular Catenanes, Rotaxanes and Knots* (VCH-Wiley, Weinheim, 1999).
10. Gatti, F. G. *et al.* Stiff, and sticky in the right places: The dramatic influence of preorganizing guest binding sites on the hydrogen bond-directed assembly of rotaxanes. *J. Am. Chem. Soc.* **123,** 5983–5989 (2001).
11. Gatti, F. G. *et al.* Photoisomerization of a rotaxane hydrogen bonding template: Light-induced acceleration of a large amplitude rotational motion. *Proc. Natl Acad. Sci. USA* **100,** 10–14 (2003).
12. Altieri, A. *et al.* Remarkable positional discrimination in bistable, light and heat-switchable, hydrogen bonded molecular shuttles. *Angew. Chem. Int. Edn* **42,** 2296–2300 (2003).
13. Yasuda, R., Noji, H., Kinosita, K. Jr & Yoshida, M. F_1-ATPase is a highly efficient molecular motor that rotates with discrete 120° steps. *Cell* **93,** 1117–1124 (1998).
14. Frkanec, L., Jokić, M., Makarević, J., Wolsperger, K. & Žinić, M. Bis(PheOH) maleic acid amide-fumaric acid amide photoisomerization induces microsphere-to-gel fibre morphological transition: A photoinduced gelation system. *J. Am. Chem. Soc.* **124,** 9716–9717 (2002).
15. Feynman, R., Leighton, R. B. & Sands, M. L. *The Feynman Lectures on Physics* Vol. 1, Ch. 46 (Addison-Wesley, Reading, MA, 1963).
16. Davis, A. P. Tilting at windmills? The second law survives. *Angew. Chem. Int. Edn* **37,** 909–910 (1998).
17. Brouwer, A. M. *et al.* Photoinduction of fast, reversible translational motion in a hydrogen-bonded molecular shuttle. *Science* **291,** 2124–2128 (2001).
18. Kelly, T. R. *et al.* A molecular brake. *J. Am. Chem. Soc.* **116,** 3657–3658 (1994).
19. Trnka, T. M. & Grubbs, R. H. The development of L_2X_2Ru = CHR olefin metathesis catalysts: An organometallic success story. *Acc. Chem. Res.* **34,** 18–29 (2001).

Supplementary Information accompanies the paper on **www.nature.com/nature**.

Acknowledgements We thank E. M. Perez for developing the catalytic Br_2 reaction conditions and P. J. Nash for several of the model [2]rotaxanes. This work was carried out through the support of the RTN network EMMMA and the FET MechMol. D.A.L. is an EPSRC Advanced Research Fellow.

Competing interests statement The authors declare that they have no competing financial interests.

Correspondence and requests for materials should be addressed to D.A.L. (David.Leigh@ed.ac.uk).

Post-earthquake ground movements correlated to pore-pressure transients

Sigurjón Jónsson*, Paul Segall†, Rikke Pedersen‡ & Grímur Björnsson§

** Department of Earth and Planetary Sciences, Harvard University, 20 Oxford Street, Cambridge, Massachusetts 02138, USA*
† Department of Geophysics, Stanford University, Stanford, California 94305-2215, USA
‡ Nordic Volcanological Institute, Grensásvegur 50, and § National Energy Authority, Grensásvegur 9, 108 Reykjavík, Iceland

Large earthquakes alter the stress in the surrounding crust, leading to triggered earthquakes and aftershocks[1–3]. A number of time-dependent processes, including afterslip, pore-fluid flow and viscous relaxation of the lower crust and upper mantle, further modify the stress and pore pressure near the fault, and hence the tendency for triggered earthquakes[4,5]. It has proved difficult, however, to distinguish between these processes on the basis of direct field observations, despite considerable effort[6]. Here we present a unique combination of measurements consisting of satellite radar interferograms[7] and water-level changes in geothermal wells following two magnitude-6.5 earthquakes in the south Iceland seismic zone. The deformation recorded in the interferograms cannot be explained by either afterslip or viscoelastic relaxation, but is consistent with rebound of a porous elastic material in the first 1–2 months following the earthquakes. This interpretation is confirmed by direct measurements which show rapid (1–2-month) recovery of the earthquake-induced water-level changes. In contrast, the duration of the aftershock sequence is projected to be ~3.5 years, suggesting that pore-fluid flow does not control aftershock duration. But because the surface strains are dominated by pore-pressure changes in the shallow crust, we cannot rule out a longer pore-pressure transient at the depth of the aftershocks. The aftershock duration is consistent with models of seismicity rate variations based on rate- and state-dependent friction laws.

The south Iceland seismic zone (SISZ) is a left-lateral transform

© 2003 Nature Publishing Group

zone connecting two sections of the mid-Atlantic plate boundary (Fig. 1), where east–west transform motion is accommodated by north–south-oriented right-lateral faults[8]. This region has suffered more than 30 large earthquakes during the past 800 years[9]. The earthquakes on 17 and 21 June 2000 ruptured two of these faults, separated by 17 km (refs 10–12) (Fig. 1). Large earthquakes in the SISZ typically cluster in time; five or six large earthquakes occurred during a period of only two weeks in 1896 (ref. 13). The last major earthquake occurred in 1912, and the time interval between sequences is 45–112 years (ref. 13).

Satellite radar interferograms (InSAR)[7] of the SISZ exhibit a quadrantal pattern of post-seismic deformation following the June 2000 earthquakes. The interferograms show several centimetres of LOS (line of sight between the ground and the satellite radar) displacement that is opposite in sense to that from right-lateral coseismic fault slip (Fig. 2 and ref. 11). An interferogram spanning the time interval from 19 June 2000 (between the two earthquakes) to 24 July 2000 shows localized deformation near the eastern, 17 June rupture (Fig. 2a). Following the earthquakes, the ground moved up towards the satellite radar in quadrants of coseismic extension (northeast and southwest of the fault) and away in quadrants of coseismic compression (northwest and southeast of the fault). The largest LOS displacement is observed northwest of the fault (−3.5 cm), while the two quadrants to the south exhibit smaller signals. Two other post-seismic interferograms exhibit similar deformation near the 17 June rupture (Fig. 2f, g). These interferograms also show LOS ground displacements up towards (away from) the satellite radar, northeast (northwest) of the 21 June rupture, but only LOS displacements away from the radar near the southern end of the fault. A fourth interferogram, spanning 35 days from 12 August to 16 September shows little or no deformation (Fig. 2e). Therefore, the post-seismic deformation was a transient that lasted about 2 months.

Post-seismic deformation can be caused by: (1) creep (afterslip) on or adjacent to the mainshock rupture[14]; (2) visco-elastic relaxation in the lower crust and upper mantle driven by stresses induced by the mainshock[6]; (3) poro-elastic rebound due to pore-fluid flow in response to mainshock induced pore-pressure changes[15]. We show here that the SISZ post-seismic deformation is consistent with poro-elastic rebound, but inconsistent with both afterslip and visco-elastic relaxation.

The observed post-seismic LOS displacements are opposite in sense to those from right-lateral strike slip. If the observed signals were due to creep, as initially was suggested[10], the slip would require left-lateral backslip with a significant component of vertical slip. The latter is unlikely on these near-vertical faults because no vertical slip occurred coseismically[11]. Although the 21 June earthquake altered the stress on the 17 June fault, these changes do not favour backslip, as the calculated Coulomb failure stress changes have the wrong sign to encourage such slip.

Viscous flow of the lower crust or upper mantle is also not a plausible explanation. The short duration of the deformation transient would require a viscosity of the order of 10^{17} Pa s (relaxation time of 2–3 weeks), which is much lower than viscosity estimates for the lower crust and upper mantle in Iceland; these estimates range from 1×10^{18} to 5×10^{19} Pa s (refs 16–19). Even though the viscosity may be low initially after a large stress change[6], a lower-crustal or upper-mantle origin of the signals cannot be reconciled with the limited spatial extent of the observed deformation, which is concentrated within 5–10 km of the faults (Fig. 2a, d).

Large earthquakes cause pore-pressure increase in areas of

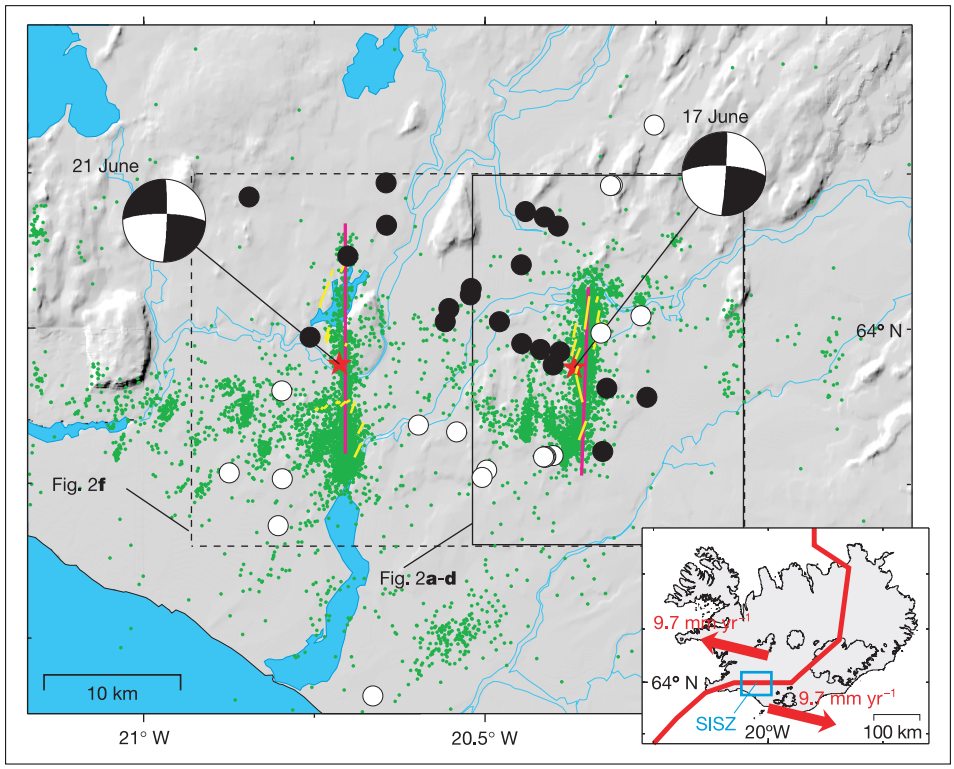

Figure 1 Map showing the location of the two June 2000 (moment magnitude $M_w = 6.5$) earthquakes in south Iceland. Inset, the approximate location of the mid-Atlantic plate boundary in Iceland, which has a full spreading rate of 1.94 cm yr^{-1} (ref. 25). The south Iceland seismic zone (SISZ) is an east–west-oriented left-lateral transform zone (small blue box marks area shown in detail). The map shows mainshock epicentres (red stars) and focal mechanisms (Harvard CMT[26]), other earthquakes from 21 June to 31 December 2000 (green dots), mapped surface ruptures[22] (yellow lines), and model fault traces as estimated from an inversion of the coseismic GPS and InSAR data for fault geometry[11] (purple lines). Also shown is the 17 June coseismic water-level increase (black dots) and decrease (white dots) in geothermal wells in the area[20]. Note water-level increase in compressional quadrants. Solid rectangle marks the area shown in Fig. 2a–d and the larger dashed rectangle the area covered in Fig. 2f.

© 2003 Nature Publishing Group

compression and decrease in areas of dilation[5,20]. These pore-pressure gradients induce groundwater flow and additional time-dependent strain[21]. This poro-elastic rebound results in subsidence within (coseismic) compressional quadrants and uplift in (coseismic) extensional quadrants. Assuming complete equilibration of the pore-pressure gradients yields a quadrantal deformation pattern similar to the observations, especially near the 17 June rupture (Fig. 2b). Although modelled displacements capture the main features of the interferometric signals, some differences are evident. Observed deformation near the southern end of the 17 June rupture is weaker than at the northern end, indicating either spatially variable material properties or local rebound that occurred so rapidly it was not detected. The southern end of the 21 June rupture, an area of very complex surface faulting, exhibits only subsidence (Fig. 2f). Complications here include local conjugate east–west-oriented left-lateral faulting[22]. In contrast, the poro-elastic computations are based on a single vertical north–south fault.

Poro-elastic rebound has previously been inferred from InSAR measurements following the 1992 Landers earthquake[15]. We find direct confirmation of pore-pressure recovery using water-level changes observed in numerous geothermal wells in the SISZ. The sign of the coseismic water-level changes exhibits a quadrantal pattern, consistent with the predicted undrained response (Figs 1 and 3a). Water-level changes reverse sign in the post-seismic period (Fig. 3b). Although there is some variability between wells, the duration of the water-level recovery is typically 1–2 months, consistent with the duration of the deformation transient (Fig. 4a). Interestingly, the two wells located just south of the 17 June fault show faster water-level recovery, indicating high permeability[20] (see well HR in Fig. 4a). This suggests that the weak deformation signal observed in this area resulted from a fast rebound that was not captured by the interferograms. The initial images were acquired 2 days (Fig. 2a) and 7 days (Fig. 2f) after the 17 June earthquake.

Competing models for the time-dependent decay of aftershocks include changes in fault strength due to poro-elastic relaxation[5], and delayed slip instabilities due to rate- and state-dependent friction on faults stressed by the mainshock[2]. We now consider if the unique measurements collected following the June 2000 earthquakes allow us to discriminate between these models.

Off-fault aftershocks preferentially occur in quadrants that experienced decreases in pore-pressure and fault-normal extension on north–south-oriented faults, that is, northeast and southwest of the faults (Fig. 1). Post-seismic pore-fluid flow would raise pore pressure in those quadrants, bringing the faults closer to failure. However, the duration of the aftershock sequence is much longer (~3.5 years) than the duration of the observed pore-pressure transients (Fig. 4b), suggesting that pore-pressure recovery is not the controlling mechanism. On the other hand, the permeability at the 3–10-km depth of the aftershocks is likely to be less than that at

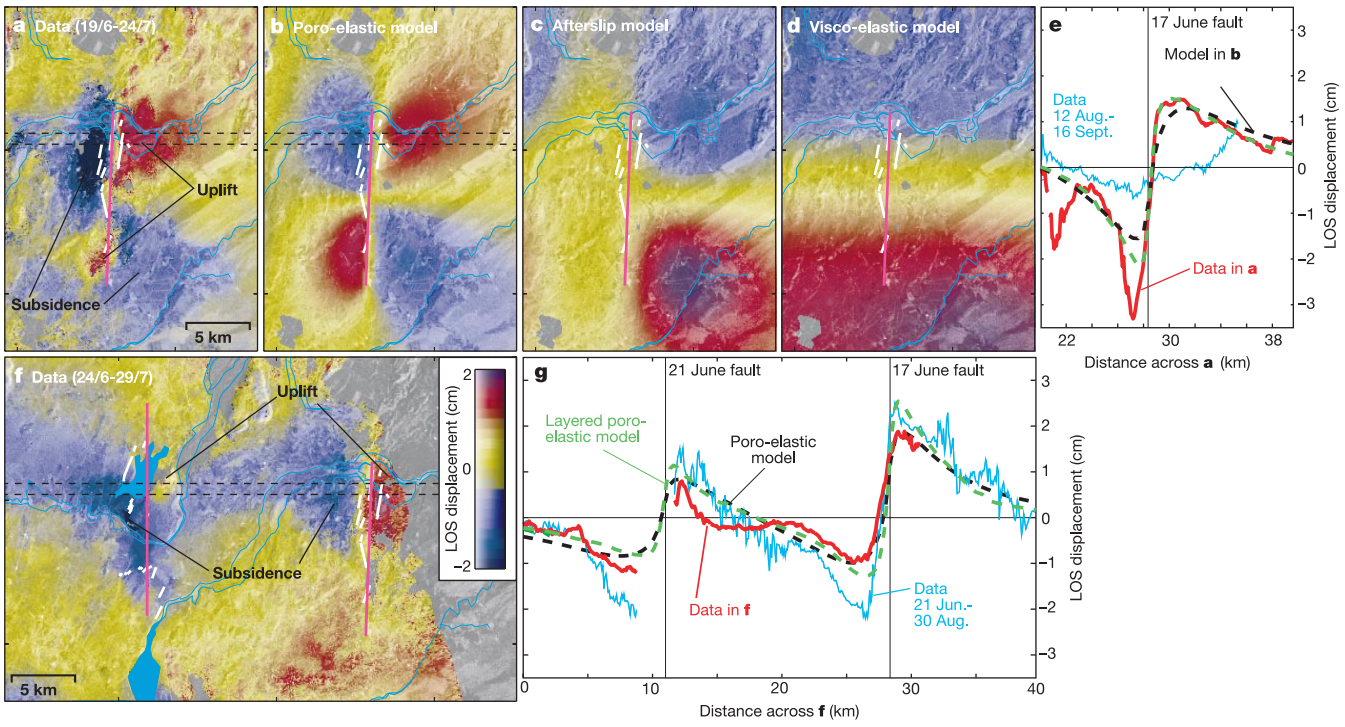

Figure 2 Synthetic aperture radar interferograms (InSAR) showing observed and simulated post-seismic deformation in south Iceland. The interferograms are unwrapped[27], and show ground displacements in the line of sight (LOS) towards the European radar satellite ERS-2 (range decrease is shown positive). The measurement is most sensitive to vertical ground motion, as the LOS vectors are roughly [east, north, up] = [0.38, −0.11, 0.92] for image **a** acquired from a descending orbit and [−0.41, −0.11, 0.90] for image **f** from an ascending orbit. The post-seismic interferograms span **a**, 19 June to 24 July (track 95, frame 2313) and **f**, 24 June to 29 July (track 173, frame 1287). In **a**, coseismic deformation caused by the 21 June earthquake, 17 km to the west, has been removed using a fault-slip model[11]. Also shown are simulated interferograms of post-seismic deformation using poro-elastic (**b**), right-lateral afterslip (**c**), and visco-elastic (**d**) models. The poro-elastic model prediction, **b**, is calculated using an undrained Poisson's ratio ν_u of 0.31 and a drained Poisson's ratio ν of 0.27 (refs 15, 24, 28), as well as the coseismic slip distribution for the two earthquakes[11]. The afterslip model assumes up to 50 cm of right-lateral slip centred at 8 km depth. The visco-elastic model has a 10-km-thick elastic crust overlying a visco-elastic half-space with viscosity of 10^{17} Pa s, chosen to match the time duration of the observed deformation transient. In **e** and **g** the average of LOS displacements profiles (between dashed lines) for interferograms in **a** and **f** are shown, as well as for two other interferograms (not shown) spanning the time intervals from 21 June (22 h after the 21 June earthquake) to 30 August (ascending track 130, frame 1287), and 12 August to 16 September (descending track 367, frame 2313). The response from a layered poro-elastic model (green dashed line), with drainage in only the top 1.5 km of the crust (see Methods section), shows similar response as the homogenous model (black dashed line and **b**) when the difference of the Poisson's ratios ($\nu_u - \nu$) is scaled (here by 2).

© 2003 Nature Publishing Group

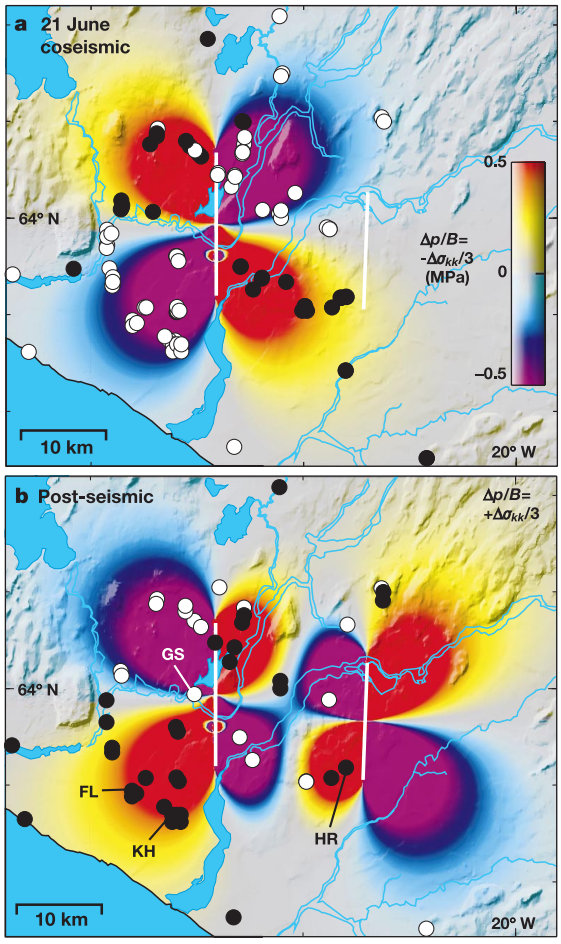

Figure 3 Coseismic and post-seismic water-level changes in geothermal wells in south Iceland. **a**, The 21 June coseismic water-level increase (black dots) and decrease (white dots) as well as the predicted coseismic pore-pressure change at 0.5 km depth (normalized by B: $\Delta p/B = -\Delta\sigma_{kk}/3$). **b**, Post-seismic water-level changes after 21 June and predicted post-seismic pore-pressure changes ($\Delta p/B = +\Delta\sigma_{kk}/3$). Water-level changes in labelled wells are shown as functions of time in Fig. 4a.

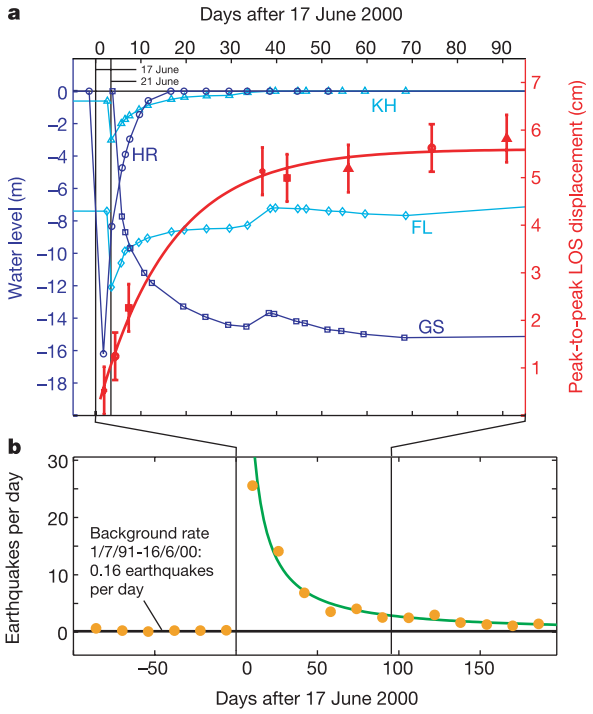

Figure 4 Water-level recoveries and aftershock decay in south Iceland. **a**, Observed peak-to-peak LOS displacement (red symbols) across the 17 June fault in several interferograms indicates that the post-seismic deformation transient lasted 2 months. Water-level changes (blue lines) show similar recovery of 1–2 months (well locations are shown in Fig. 3b). Well GS (squares) is located in coseismic compressional quadrants and experiences post-seismic water-level decline, whereas wells KH (triangles), FL (diamonds) and HR (circles) are located in coseismic extensional quadrants and exhibit post-seismic water-level increase. Note the rapid water-level recovery of well HR, located just south of the 17 June fault. **b**, Aftershock decay after the 17 June earthquake showing much longer timescale. Extrapolation of the ongoing aftershock sequence within 5 km of the 17 June fault predicts a total duration of 3.5 years. Same analysis for the 21 June fault-zone predicts aftershock duration of 3.3 years.

the <1.5-km depth of the geothermal wells. To test whether the observed surface displacements might have been caused by shallow drainage, and would thus permit pore pressures at depth to decay on a timescale commensurate with the aftershocks, we computed the surface deformation for an end-member layered model. In this calculation, the permeability between the surface and depth D is infinite, and the earthquake-induced pore pressures relax instantaneously. Below D, the permeability is zero and there is no drainage. We computed the predicted range change due to complete draining of the highly permeable near-surface rocks by integrating the point source response from the surface to depth D (see Methods). Figure 2e and g shows that by adjusting the difference between undrained and drained Poisson's ratios ($\nu_u - \nu$), it is possible to fit the observations with only the shallow rocks draining. Thus, at this point, we cannot rule out deep pore-pressure changes on the timescale of the aftershocks.

Mainshock stress changes accelerate nucleation patches on neighbouring faults to instability. It has been shown that the time-to-instability relations, for fault patches subject to rate- and state-dependent friction, yield Omori-like aftershock decay where earthquake rate decreases as 1/time (ref. 2). This model predicts that aftershock duration t_a is proportional to $A\sigma$, and inversely proportional to the background stressing rate. Here A is an experimentally determined fault constitutive parameter (0.005–0.02 for most rocks) and σ is effective normal stress. Assuming that the background stressing rate can be approximated by earthquake stress drop $\Delta\tau$ divided by average recurrence interval t_r leads to $t_a = t_r A\sigma/\Delta\tau$. For the SISZ, where similar events recur roughly every 100 years, this model predicts an aftershock duration of 2.5–10 years (for $\Delta\tau/A\sigma$ of 10–40), which is in good accord with the observed aftershock decay.

We conclude that poro-elastic rebound dominates the post-seismic deformation in the first few months after the earthquakes. Pore pressures in the shallow crust equilibrate too rapidly to explain the observed aftershock decay, but we cannot at present rule out longer-term pore-pressure transients in lower-permeability rocks at the depths of most aftershocks. The data are consistent with aftershock duration being controlled by time-dependent failure of faults stressed by the mainshock. □

Methods

Here we explain how surface displacements due to complete draining of a permeable surface layer are calculated. Pore-pressure changes Δp induce surface displacements u_i given by

$$u_i(x) = \frac{3(\nu_u - \nu)}{B(1+\nu_u)(1-2\nu)} \int \Delta p(\xi) \frac{\partial g_i^k(x,\xi)}{\partial \xi_k} dV_\xi \qquad (1)$$

where ν and ν_u are the drained and undrained Poisson's ratios, B is Skempton's pore-pressure coefficient, and g_i^k is the elastic Green's function—that is, the displacement at x in the i-direction due to a point force in the k-direction at ξ (refs 23, 24). The pore-pressure change induced by dissipation of the undrained pore pressures is $B\Delta\sigma_{kk}/3$, where $\Delta\sigma_{kk}/3$ is

© 2003 Nature Publishing Group

the coseismic mean stress change. For a homogeneous half-space we have

$$\frac{\partial g_i^k(x,\xi)}{\partial \xi_k} = \frac{(1-2\nu)}{2\pi\mu}\frac{x_i-\xi_i}{R^3} \quad (2)$$

where μ is shear modulus, and R is the euclidean distance between x and ξ. Therefore, equation (1) can be written as:

$$u_i(x) = \frac{(\nu_u-\nu)}{2\pi\mu(1+\nu_u)}\int \Delta\sigma_{kk}(\xi)\frac{x_i-\xi_i}{R^3}dV_\xi. \quad (3)$$

To determine surface displacements due to complete draining of a permeable surface layer with thickness D, overlying impermeable rocks, we integrate equation (3) from the surface to depth D. Note that equation (3) scales with $(\nu_u - \nu)$.

Received 23 January; accepted 23 May 2003; doi:10.1038/nature01776.

1. Harris, R. A., Simpson, R. W. & Reasenberg, P. A. Influence of static stress changes on earthquake locations in southern California. *Nature* **375,** 221–224 (1995).
2. Dieterich, J. A constitutive law for rate of earthquake production and its application to earthquake clustering. *J. Geophys. Res.* **99,** 2601–2618 (1994).
3. Toda, S., Stein, R. S. & Sagiya, T. Evidence from the AD 2000 Izu islands earthquake swarm that stressing rate governs seismicity. *Nature* **419,** 58–61 (2002).
4. Freed, A. M. & Lin, J. Delayed triggering of the 1999 Hector Mine earthquake by viscoelastic stress transfer. *Nature* **411,** 180–183 (2001).
5. Nur, A. & Booker, J. R. Aftershocks caused by pore fluid flow? *Science* **175,** 885–887 (1972).
6. Pollitz, F. F., Wicks, C. & Thatcher, W. Mantle flow beneath a continental strike-slip fault: Post-seismic deformation after the 1999 Hector Mine earthquake. *Science* **293,** 1814–1818 (2001).
7. Zebker, H., Rosen, P., Goldstein, R., Gabriel, A. & Werner, C. On the derivation of coseismic displacement fields using differential radar interferometry: The Landers earthquake. *J. Geophys. Res.* **99,** 19617–19643 (1994).
8. Einarsson, P. Earthquakes and present-day tectonism in Iceland. *Tectonophysics* **189,** 261–279 (1991).
9. Einarsson, P. & Eiríksson, J. Earthquake fractures in the Districts Land and Rangárvellir in the South Iceland Seismic Zone. *Jökull* **32,** 113–119 (1982).
10. Pedersen, R., Sigmundsson, F., Feigl, K. L. & Árnadóttir, T. Coseismic interferograms of two $M_S = 6.6$ earthquakes in the South Iceland Seismic Zone, June 2000. *Geophys. Res. Lett.* **28,** 3341–3344 (2001).
11. Pedersen, R., Jónsson, S., Árnadóttir, T., Sigmundsson, F. & Feigl, K. Fault slip distribution of two June 2000 $M_w = 6.5$ earthquakes in South Iceland estimated from joint inversion of InSAR and GPS measurements. *Earth Planet. Sci. Lett.* (in the press).
12. Árnadóttir, T. *et al.* Crustal deformation measured by GPS in the South Iceland Seismic Zone due to two large earthquakes in June 2000. *Geophys. Res. Lett.* **28,** 4031–4033 (2001).
13. Einarsson, P., Björnsson, S., Foulger, G., Stefánsson, R. & Skaftadóttir, Th. in *Earthquake Prediction—An International Review* Vol. 4 (eds Simpson, D. W. & Richards, P. G.) 141–151 (American Geophysical Union, Washington DC, 1981).
14. Bürgmann, R. *et al.* Time-space variable afterslip on and deep below the Izmit earthquake rupture. *Bull. Seismol. Soc. Am.* **92,** 126–137 (2002).
15. Peltzer, G., Rosen, P., Rogez, F. & Hudnut, K. Poro-elastic rebound along the Landers 1992 earthquake surface rupture. *J. Geophys. Res.* **103,** 30131–30145 (1998).
16. Sigmundsson, F. Post-glacial rebound and asthenosphere viscosity in Iceland. *Geophys. Res. Lett.* **18,** 1131–1134 (1991).
17. Sigmundsson, F. & Einarsson, P. Glacio-isostatic crustal movements caused by historical volume change of the Vatnajokull ice cap, Iceland. *Geophys. Res. Lett.* **19,** 2123–2126 (1992).
18. Pollitz, F. F. & Sacks, I. S. Viscosity structure beneath northeast Iceland. *J. Geophys. Res.* **101,** 17771–17793 (1996).
19. Hofton, M. & Foulger, G. R. Postrifting anelastic deformation around the spreading plate boundary, north Iceland: 1. Modeling of the 1987-1992 deformation field using a visco-elastic earth structure. *J. Geophys. Res.* **101,** 25403–25421 (1996).
20. Björnsson, G., Flovenz, Ó. G., Saemundsson, K. & Einarsson, E. H. in *Proc. 26th Workshop on Geothermal Reservoir Engineering* SGP-TR-168, 327–334 (Stanford University, Stanford, 2001).
21. Roeloffs, E. Poroelastic techniques in the study of earthquake-related hydrologic phenomena. *Adv. Geophys.* **27,** 135–195 (1996).
22. Clifton, A. & Einarsson, P. in *Autumn Meeting 2000—Abstracts* (ed Jónsson, S. S.) 1 (Geoscience Society of Iceland, Reykjavík, 2000).
23. Segall, P. Induced stresses due to fluid extraction from axisymmetric reservoirs. *Pure Appl. Geophys.* **139,** 535–560 (1992).
24. Rice, J. R. & Cleary, M. P. Some basic stress diffusion solutions for fluid-saturated elastic porous media with compressible constituents. *Rev. Geophys. Space Sci.* **14,** 227–241 (1976).
25. DeMets, C., Gordon, R. G., Argus, D. F. & Stein, S. Current plate motions. *Geophys. J. Int.* **101,** 425–478 (1990).
26. Dziewonski, A. M., Ekstrom, G. & Maternovskaya, N. Centroid-moment tensor solutions for April-June 2000. *Phys. Earth Planet. Inter.* **123,** 1–14 (2001).
27. Chen, C. W. & Zebker, H. A. Two-dimensional phase unwrapping with use of statistical models for cost functions in nonlinear optimization. *J. Opt. Soc. Am.* **18,** 338–351 (2001).
28. Wang, H. F. *Theory of Linear Poro-Elasticity with Applications to Geomechanics and Hydrogeology* (Princeton Univ. Press, Princeton, 2001).

Acknowledgements We thank the European Space Agency for providing the SAR data. We also thank G. Guðmundsson and R. Stefánsson for providing preliminary earthquake locations from the South Iceland Lowland (SIL) seismic network; A. Clifton and P. Einarsson for providing data of the mapped surface ruptures; F. Sigmundsson, T. Árnadóttir, K. Ágústsson, E. Roeloffs and K. Feigl for discussions; and R. Bürgmann for comments and suggestions that improved the paper.

Competing interests statement The authors declare that they have no competing financial interests.

Correspondence and requests for materials should be addressed to S.J. (sj@eps.harvard.edu).

Urbanization effects on tree growth in the vicinity of New York City

Jillian W. Gregg*‡, Clive G. Jones† & Todd E. Dawson*‡

* *Ecology and Evolutionary Biology, Cornell University, Ithaca, New York 14853, USA*

† *Institute of Ecosystem Studies, Millbrook, New York 12545, USA*

Plants in urban ecosystems are exposed to many pollutants and higher temperatures, CO_2 and nitrogen deposition than plants in rural areas[1–5]. Although each factor has a detrimental or beneficial influence on plant growth[6], the net effect of all factors and the key driving variables are unknown. We grew the same cottonwood clone in urban and rural sites and found that urban plant biomass was double that of rural sites. Using soil transplants, nutrient budgets, chamber experiments and multiple regression analyses, we show that soils, temperature, CO_2, nutrient deposition, urban air pollutants and microclimatic variables could not account for increased growth in the city. Rather, higher rural ozone (O_3) exposures reduced growth at rural sites. Urban precursors fuel the reactions of O_3 formation, but NO_x scavenging reactions[7] resulted in lower cumulative urban O_3 exposures compared to agricultural and forested sites throughout the northeastern USA. Our study shows the overriding effect of O_3 despite a diversity of altered environmental factors, reveals 'footprints' of lower cumulative urban O_3 exposures amidst a background of higher regional exposures, and shows a greater adverse effect of urban pollutant emissions beyond the urban core.

Urbanization of the globe is accelerating, with potentially large impacts on vegetation in cities and surrounding areas[8]. Urban air contains high concentrations of many gaseous, particulate and photochemical pollutants (such as NO_x, HNO_3, SO_2, H_2SO_4, O_3 and volatile organic compounds)[1,5,6]; and urban soils are high in heavy metals and can be more hydrophobic and acidic than surrounding rural environments[2]. Although many of these contaminants have detrimental effects on plant growth, urban environments also have higher rates of nutrient and base-cation deposition[1,5], warmer temperatures (urban 'heat-island' effect)[3] and increased CO_2 concentrations[4]—factors that often, but not invariably, enhance plant growth. Given the potential for interactions among all factors[9] and the relative absence of studies examining more than two or three factors in combination, understanding the net effect of multiple anthropogenic environmental changes in an urban environment and the relative importance of the individual factors remains a major challenge.

We used an inherently fast-growing clone of Eastern cottonwood (*Populus deltoides*) as a 'phytometer'[10] to integrate the net growth response to multiple anthropogenic environmental changes in New York City compared to surrounding rural environments. Rapid growth rates, continuous growth throughout the season, and responsiveness to a range of climatic and pollutant variables[11–15] make this widespread riparian and early successional tree species a suitable indicator. Soil transplants, nutrient budgets, chamber replication of field conditions and multiple regression approaches were then used to determine the key driving variables. Urban and rural site comparisons were selected from known steep pollution gradients[1,16] across relatively short spatial scales (~100 km). Local variation in light and precipitation was minimized by growing plants in open fields with drip irrigation. Temperature effects on season length were controlled by synchronizing transplant and

‡ Present addresses: US EPA Western Ecology Division, Corvallis, Oregon 97333, USA (J.W.G.); Department of Integrative Biology, University of California, Berkeley, California 94720, USA (T.E.D.).

© 2003 Nature Publishing Group